

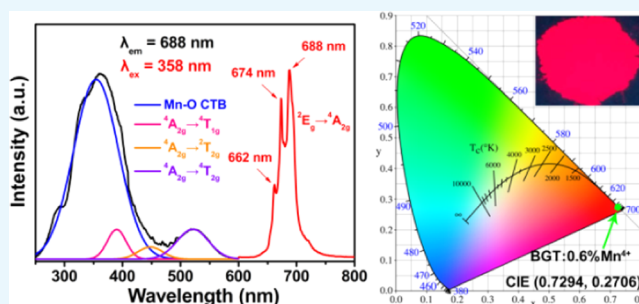
Synthesis, Crystal Structure, and Photoluminescence Characteristics of High-Efficiency Deep-Red Emitting Ba₂GdTaO₆:Mn⁴⁺ Phosphors

Qi Sun,[†] Shaoying Wang,[†] Balaji Devakumar,[†] Liangling Sun,[†] Jia Liang,[†] and Xiaoyong Huang^{*,†,‡}

[†]College of Physics and Optoelectronics, Taiyuan University of Technology, Taiyuan 030024, P. R. China

[‡]Institute for Advanced Study, Shenzhen University, Nanhai Avenue 3688, Shenzhen 518060, P. R. China

ABSTRACT: In this article, a series of novel Mn⁴⁺-doped Ba₂GdTaO₆ (BGT) red-emitting phosphors were successfully synthesized via a high-temperature solid-state method. The crystal structure, morphology, and luminescent performance of the samples were investigated in detail with X-ray diffraction, field emission scanning electron microscopy, photoluminescence (PL) spectra, decay curves, and internal quantum efficiency (IQE). Excited at 358 nm, these samples showed an intense deep-red emission band peaking at 688 nm in the wavelength region of 620–800 nm. The excitation spectra of these samples monitored at 688 nm exhibited two broad excitation bands from 250 to 600 nm with peaks at 358 and 469 nm. The systematic investigation of the concentration-dependent PL properties of BGT:Mn⁴⁺ phosphors revealed that the deep-red emission intensity reached the maximum when the Mn⁴⁺ doping concentration was 0.6 mol %. The critical distance (R_c) between Mn⁴⁺ ions for concentration quenching was 36.57 Å, and the major mechanism of energy transfer among Mn⁴⁺ activators in BGT:Mn⁴⁺ was dipole–dipole interaction. The decay lifetimes decreased from 0.285 to 0.248 ms with the increasing Mn⁴⁺ doping concentration from 0.2 to 1.2 mol %. The Commission Internationale de l'Éclairage coordinates of the optimal BGT:0.6%Mn⁴⁺ sample were (0.7294, 0.2706). The values of the IQE for all BGT:Mn⁴⁺ samples were measured, and the highest value could reach up to 62%. The above results revealed that these high-efficiency BGT:Mn⁴⁺ deep-red-emitting phosphors had promising potential for application in indoor plant growth lighting.



1. INTRODUCTION

It is well known that light is the basic factor of plant growth and development.¹ Light can not only provide the energy needed for plant photosynthesis but also regulate plant life activities, such as seed germination, seedling formation, flowering, bearing, and other processes.² Therefore, plant illumination technology is an indispensable part of modern agricultural development; especially for areas lacking land resources and light conditions, plant illumination is particularly important.³ As reported previously, the blue light around 450 nm (410–500 nm) and red light around 660 nm (610–700 nm) are important for photosynthesis, phototropism, and photomorphogenesis.^{4–7} At present, the light-emitting diodes (LEDs) possess many advantages, such as energy savings, low cost, high efficiency, environmental friendliness, and long lifetimes, and could be considered as the main type of light source for both general lighting and plant growth lighting.^{8–18} According to the current situation, searching for phosphors with bright red emission for plant growth lighting is imperative.

Recently, non-rare-earth transitional-metal Mn⁴⁺ ions, which could serve as efficient luminescent activators with a strong absorption in the range of 250–600 nm and an intense red emission covering the region from 600 to 800 nm, were widely investigated for developing new red phosphors.^{3,5,19–30} Generally, Mn⁴⁺ ions can be stable in the host matrix with

an octahedral environment.^{31–33} Double perovskite structure is regarded as an outstanding host material for Mn⁴⁺ activators on account of its different crystal structures, excellent optical properties, and good chemical stability.^{34–36} Previously, our group has reported several red phosphors based on Mn⁴⁺-activated double perovskite compounds, including Ca₂GdTaO₆:Mn⁴⁺, KLaMgWO₆:Mn⁴⁺, NaLaMgWO₆:Mn⁴⁺, BaLaMgSbO₆:Mn⁴⁺, Ca₂GdSbO₆:Mn⁴⁺, and BaLaMgNbO₆:Mn⁴⁺.^{34,37–41} To the best of our knowledge, the luminescence properties of the Mn⁴⁺-doped Ba₂GdTaO₆ (BGT) double perovskite have not been reported until now. The BGT compound would be a good host material for Mn⁴⁺ ion doping because it has abundant [TaO₆] octahedrons that are favorable for Mn⁴⁺ ions to replace Ta⁵⁺ ion sites.⁴² Accordingly, in this work, we reported on the luminescence properties of BGT:Mn⁴⁺ phosphors, which were synthesized using the conventional high-temperature solid-state reaction method. The crystal structure, morphology, optical properties, decay curves, and internal quantum efficiency (IQE) of the BGT:Mn⁴⁺ phosphors were systematically investigated and discussed. Our results demonstrated that the as-prepared

Received: June 16, 2019

Accepted: July 24, 2019

Published: August 6, 2019

BGT:Mn⁴⁺ phosphors were efficient deep-red-emitting luminescent materials for indoor plants growth LEDs.

2. RESULTS AND DISCUSSION

The X-ray diffraction (XRD) patterns of the BGT:*x*Mn⁴⁺ (*x* = 0.2, 0.6, and 1.2 mol %) samples are displayed in Figure 1. It

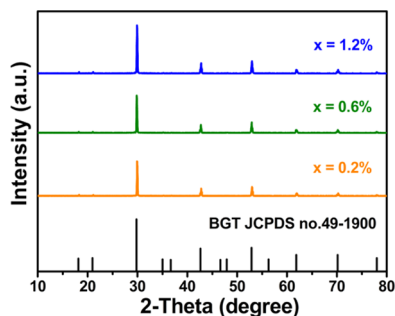


Figure 1. XRD patterns of BGT:*x*Mn⁴⁺ (*x* = 0.2, 0.6, and 1.2%) phosphors and the standard diffraction positions of the BGT compound (JCPDS no. 49-1900).

could be seen that all of the diffraction peaks of these samples were completely matched with those of the standard JCPDS card of the BGT compound (no. 49-1900). Furthermore, other impurity phases were not found. The experimental results indicated that single-phase BGT:Mn⁴⁺ phosphors were successfully synthesized and doping of the Mn⁴⁺ ions into the BGT host had no substantial effect on the BGT structure.

Figure 2a presents Rietveld XRD refinement of BGT:0.6% Mn⁴⁺ phosphors. The values of R_p , R_{wp} , and χ^2 were determined to be 7.74%, 11.71%, and 0.5308, respectively. The results implied that the refined results were of good quality. Figure 2b shows the crystal structure of the BGT:0.6% Mn⁴⁺ sample. BGT:Mn⁴⁺ was crystallized into a tetragonal system with the space group $I4/m$. The Gd³⁺ and Ta⁵⁺ ions were surrounded by six O²⁻ ions to form the [TaO₆] octahedrons. The Ba²⁺ ions were located in the middle of the gap between octahedrons. The obtained experimental cell parameters for the BGT:0.6%Mn⁴⁺ sample were calculated to be $a = b = 6.00416(6)$ Å, $c = 8.52159(16)$ Å, $\alpha = \beta = \gamma = 90^\circ$, $V = 307.202(5)$ Å³, $N = 2$. Given that the Mn⁴⁺ ions prefer to occupy the octahedral and distorted octahedral sites and the ionic radius of the Mn⁴⁺ ions ($r = 0.53$ Å, coordination number (CN) = 6) was much closer to that of the Ta⁵⁺ ions ($r = 0.64$ Å, CN = 6) than that of the Gd³⁺ ions ($r = 0.94$ Å, CN = 6), so the Mn⁴⁺ ions could easily enter the Ta⁵⁺ octahedral sites in the BGT host.⁴³

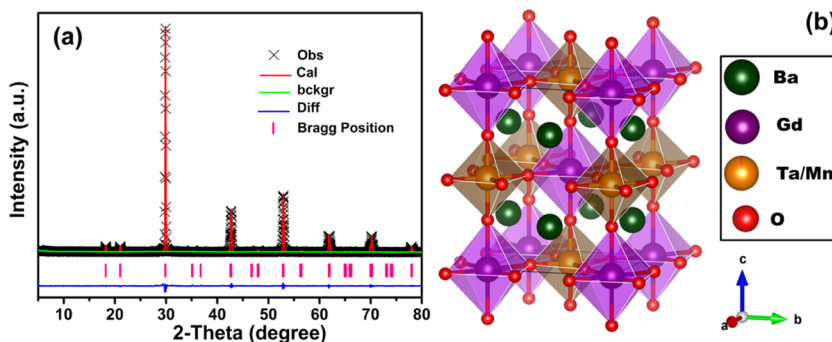


Figure 2. (a) Rietveld refinement of the XRD profiles for the BGT:0.6%Mn⁴⁺ sample. (b) Crystal structure of the BGT:0.6%Mn⁴⁺ sample.

The scanning electron microscopy (SEM) image and the corresponding elemental mapping profiles of BGT:0.6%Mn⁴⁺ phosphors are displayed in Figure 3. Obviously, the particle

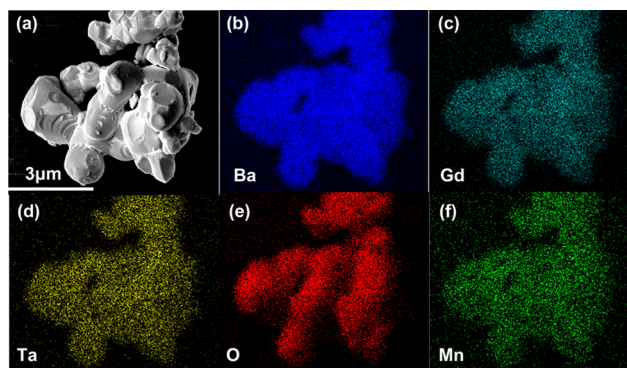


Figure 3. (a) Typical SEM image of BGT:0.6%Mn⁴⁺ phosphors. (b–f) Elemental mapping profiles of BGT:0.6%Mn⁴⁺ phosphors.

size of BGT:0.6%Mn⁴⁺ powders ranged between 1 and 3 μm, as shown in Figure 3a. The elemental mapping profiles shown in Figure 3b–f suggest that the Ba, Gd, Ta, O, and Mn elements are uniformly distributed over the whole samples.

Figure 4a exhibits the room-temperature photoluminescence (PL) and the PL excitation (PLE) spectra of the BGT:0.6%

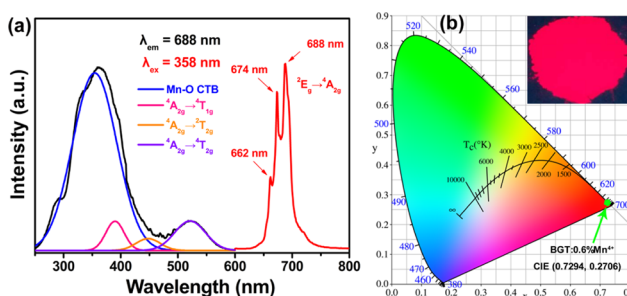


Figure 4. (a) PLE ($\lambda_{em} = 688$ nm) and PL ($\lambda_{ex} = 358$ nm) spectra of BGT:0.6%Mn⁴⁺ phosphors. (b) CIE chromaticity coordinates of BGT:0.6%Mn⁴⁺ phosphors. The inset shows the digital photograph of BGT:0.6%Mn⁴⁺ phosphors under a 365 nm UV lamp.

Mn⁴⁺ sample. The PLE spectrum recorded at 688 nm emission consisted of two broad excitation bands from 250 to 600 nm, with peaks at 358 and 469 nm. The excitation spectrum could be well-fitted into four Gaussian bands around 354, 390, 448, and 521 nm, which were attributed to the Mn–O charge-

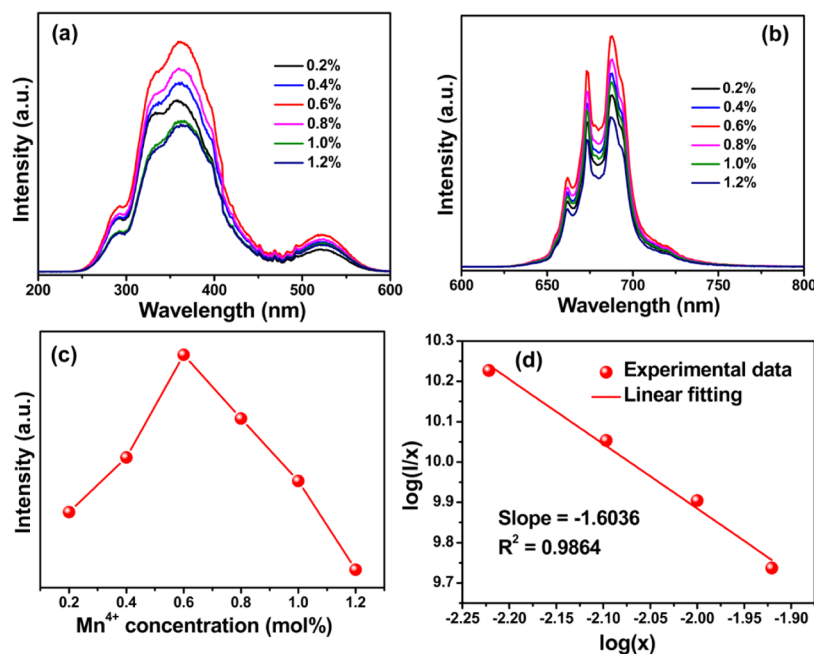


Figure 5. (a) PLE spectra of BGT: $x\text{Mn}^{4+}$ ($x = 0.2, 0.4, 0.6, 0.8, 1.0$, and 1.2 mol %) phosphors ($\lambda_{\text{em}} = 688$ nm). (b) PL spectra of BGT: $x\text{Mn}^{4+}$ ($x = 0.2, 0.4, 0.6, 0.8, 1.0$, and 1.2 mol %) phosphors under 358 nm excitation. (c) Dependence of integrated PL intensity on Mn^{4+} doping concentration in BGT: $x\text{Mn}^{4+}$ phosphors. (d) Linear fitting of $\log(I/x)$ versus $\log(x)$ in BGT: $x\text{Mn}^{4+}$ phosphors.

transfer band and the Mn^{4+} spin-allowed transitions of ${}^4\text{A}_{2g} \rightarrow {}^4\text{T}_{1g}$, ${}^4\text{A}_{2g} \rightarrow {}^2\text{T}_{2g}$, and ${}^4\text{A}_{2g} \rightarrow {}^4\text{T}_{2g}$, respectively.^{44,45} Under excitation at 358 nm, the BGT:0.6% Mn^{4+} sample exhibited an intense deep-red emission band in the wavelength range of 620–800 nm, with three emission peaks at 662, 674, and 688 nm, which can be assigned to the spin-forbidden ${}^2\text{E}_g \rightarrow {}^4\text{A}_{2g}$ transition of the Mn^{4+} ions.^{46,47} Among these emission peaks, the 688 nm emission peak showed the strongest intensity. Figure 4b shows the Commission Internationale de l'Éclairage (CIE) diagram of BGT:0.6% Mn^{4+} phosphors. The CIE chromaticity coordinates of the BGT:0.6% Mn^{4+} sample were calculated to be (0.7294, 0.2706), which were located in the deep-red region. The corresponding digital photograph of the BGT:0.6% Mn^{4+} sample under a 365 nm UV lamp is shown in the inset of Figure 4b. Clearly, the phosphors emitted bright red light.

Figure 5a shows the PLE spectra of BGT: $x\text{Mn}^{4+}$ phosphors ($x = 0.2, 0.4, 0.6, 0.8, 1.0$, and 1.2 mol %) at different Mn^{4+} doping concentrations monitored at 688 nm. It can be seen that the PLE spectra of all samples did not change significantly except for the PLE intensity. Figure 5b shows the corresponding PL spectra of the BGT: $x\text{Mn}^{4+}$ ($x = 0.2, 0.4, 0.6, 0.8, 1.0$, and 1.2 mol %) samples upon 358 nm excitation. All of the PL spectra of these samples were similar to each other except for the PL intensity. The PL intensity of BGT: $x\text{Mn}^{4+}$ phosphors increased first with increasing Mn^{4+} ion concentration, approached a maximum at $x = 0.6\%$, and then dropped as x exceeded 0.6%, as observed in Figure 5c. This phenomenon was known as the concentration quenching effect, which was caused by the energy transfer between the nearest Mn^{4+} ions.⁴⁸ The critical transfer distance (R_c) between the Mn^{4+} ions in BGT: $x\text{Mn}^{4+}$ phosphors can be estimated by the following formula^{49–51}

$$R_c \approx 2 \left[\frac{3V}{4\pi X_c N} \right]^{1/3} \quad (1)$$

where V is to the unit cell volume, X_c is the critical doping concentration, and N is the number of available sites for the dopant in the unit cell. For BGT: Mn^{4+} phosphors, $X_c = 0.6\%$, $V = 307.202(5) \text{ \AA}^3$, and $N = 2$, respectively. The R_c value was determined to be 36.57 Å, which was much higher than 5 Å. Hence, it was inferred that the energy transfer mechanism of the Mn^{4+} ions in the BGT host was dominated by the electric multipolar interaction because the exchange interaction works only at shorter distances ($R_c < 5 \text{ \AA}$).⁵² To further confirm the detailed interaction mechanism between the Mn^{4+} ions, the relationship between $\log(I/x)$ and $\log(x)$ could be expressed by the following equation⁵³

$$\frac{I}{x} = K[1 + \beta(x)^{\theta/3}]^{-1} \quad (2)$$

where I is the emission intensity of BGT: Mn^{4+} phosphors; x is the concentration of the Mn^{4+} ions; and K and β are the constants for the same excitation condition. An index of the electric multipolar character, $\theta = 6, 8$, and 10 correspond to the dipole–dipole, dipole–quadrupole, and quadrupole–quadrupole interactions, respectively.^{54–56} Figure 5d depicts the dependence of $\log(I/x)$ on $\log(x)$. It was observed that the slope of the fitted straight line ($-\theta/3$) was -1.6036 , thus the value of θ was 4.8108. The value of θ was approximately 6, suggesting that the major concentration quenching mechanism in BGT: Mn^{4+} phosphors was electric dipole–dipole reaction.

Figure 6 shows the decay curves of the 688 nm deep-red emissions of BGT: $x\text{Mn}^{4+}$ phosphors ($x = 0.2, 0.4, 0.6, 0.8, 1.0$, and 1.2 mol %) under 358 nm excitation, which could be well-fitted into double exponential decay model function below⁵⁷

$$I_t = A_1 \exp\left(-\frac{t}{\tau_1}\right) + A_2 \exp\left(-\frac{t}{\tau_2}\right) \quad (3)$$

where I_t is the luminescence intensity of BGT: $x\text{Mn}^{4+}$ phosphors at time t ; A_1 and A_2 are constants; and τ_1 and τ_2 are the short and long lifetimes for the exponential

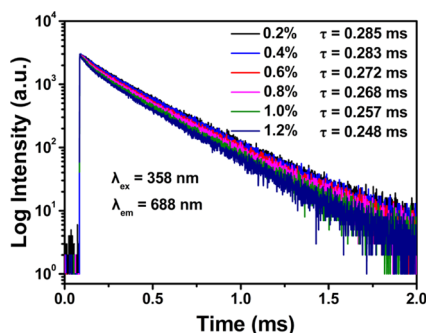


Figure 6. Decay curves and calculated lifetimes of BGT: $x\text{Mn}^{4+}$ ($x = 0.2, 0.4, 0.6, 0.8, 1.0$, and 1.2 mol %) phosphors under 358 nm excitation and monitored at 688 nm emission.

components, respectively. As a consequence, the average lifetime τ_s could be calculated by the following equation⁵⁸

$$\tau_s = (A_1\tau_1^2 + A_2\tau_2^2)/(A_1\tau_1 + A_2\tau_2) \quad (4)$$

The decay lifetimes were found to be 0.285 , 0.283 , 0.272 , 0.268 , 0.257 , and 0.248 ms for $x = 0.2, 0.4, 0.6, 0.8, 1.0$, and 1.2 mol %, respectively, as shown in Figure 6. As we can see, the values of the decay times were in the microsecond range, meaning that the luminescence was caused by the forbidden transition in the intra-d-shell of the Mn^{4+} ions.^{49,59} Distinctly, the decay times gradually decreased with x increasing from 0.2 to 1.2 mol %, which was due to the increased possibility of a nonradiative energy migration between the Mn^{4+} ions with increasing Mn^{4+} concentration.⁶⁰

Under 358 nm excitation, the IQE of the BGT: 0.6Mn^{4+} sample was measured using an integrating sphere, as shown in Figure 7a, which could be calculated by the following equation⁶¹

$$\eta = \frac{\int L_S}{\int E_R - \int E_S} \quad (5)$$

where η is the IQE; L_S is the emission spectrum of the sample; and E_S and E_R are the spectra of the excitation light with the BGT: 0.6Mn^{4+} sample and only with BaSO_4 reference, respectively. Thus, the calculated IQE was 44% , which was higher than that of the recently reported Mn^{4+} -activated red-emitting phosphors, such as $\text{Mg}_2\text{Ga}_2\text{GeO}_{12}:\text{Mn}^{4+}$ (IQE: 28.13%), $\text{La}(\text{MgTi})_{1/2}\text{O}_3:\text{Mn}^{4+}$ (IQE: 27.2%), and $\text{SrLaS-cO}_4:\text{Mn}^{4+}$ (IQE: 12.2%).^{62–64} Furthermore, we also measured the IQEs for other samples of BGT: $x\text{Mn}^{4+}$ phosphors using the

same integrating sphere method. As shown in Figure 7b, the IQE values of BGT: $x\text{Mn}^{4+}$ phosphors ($x = 0.2, 0.4, 0.6, 0.8, 1.0$, and 1.2 mol %) under 358 nm excitation were calculated to be about 62 , 52 , 44 , 41 , 32 , and 24% , respectively.

Finally, we compared the as-prepared BGT: 0.6Mn^{4+} phosphors with several reported Mn^{4+} -activated perovskite-type red-emitting phosphors. Their host materials, optimal Mn^{4+} doping concentrations, PL and PLE peaks, and IQEs are shown in Table 1. It can be seen that BGT: 0.6Mn^{4+}

Table 1. Comparison of Several Reported Mn^{4+} -Activated Perovskite-Type Red-Emitting Phosphors

hosts	concentrations (%)	PLE peak (nm)	PL peak (nm)	IQE (%)	refs
$\text{Ba}_2\text{LaSbO}_6$	0.13	360	656, 678	20.2	59
$\text{Ba}_2\text{GdSbO}_6$	0.3	350	661, 673, 687	27.7	65
Ba_2YNbO_6	0.5	350	663, 695	29.2	66
$\text{Ca}_2\text{GdTao}_6$	0.4	355	676	33	37
$\text{Ca}_2\text{LaTaO}_6$	0.4	325	696	34.6	35
$\text{Ca}_2\text{GdSbO}_6$	0.6	356	676	38.9	40
$\text{Ba}_2\text{GdTao}_6$	0.6	358	662, 674, 688	44	this work

phosphors had a higher IQE and better PL properties than other phosphors. These results further demonstrated that the as-prepared BGT: 0.6Mn^{4+} phosphors with outstanding optical properties could be applied in plant growth LEDs.

3. CONCLUSIONS

In summary, Mn^{4+} -activated BGT deep-red-emitting phosphors have been synthesized by a high-temperature solid-state reaction method. The excitation spectra showed broad excitation bands in the wavelength region of 250 – 600 nm, which matched well with the emission of the commercial near-UV LED chips. The PL spectra presented a deep-red emission band with a maximum at 688 nm. The optimized doping concentration of Mn^{4+} in the BGT host was determined to be 0.6 mol %. The critical distance (R_c) of concentration quenching was found to be 36.57 Å, and the concentration quenching phenomenon was caused by the dipole–dipole interaction-based energy transfer among the Mn^{4+} centers. The CIE chromaticity coordinates of the BGT: 0.6Mn^{4+} sample were calculated to be $(0.7294, 0.2706)$. The IQE value of BGT: Mn^{4+} phosphors reached as high as 62% . Finally, all results indicated that BGT: Mn^{4+} phosphors were potential

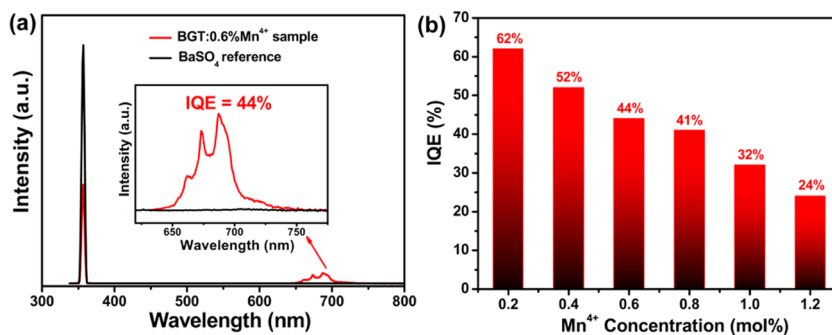


Figure 7. (a) Excitation line of BaSO_4 reference and the emission spectrum of BGT: 0.6Mn^{4+} phosphors collected using an integrating sphere. (b) IQEs of BGT: $x\text{Mn}^{4+}$ phosphors ($x = 0.2, 0.4, 0.6, 0.8, 1.0$, and 1.2 mol %) under 358 nm excitation.

candidates for deep-red phosphors for indoor plants growth LEDs.

4. EXPERIMENTAL SECTION

4.1. Sample Preparation. The powder samples with the general formula of $\text{Ba}_2\text{GdTa}_{1-x}\text{O}_6:\text{xMn}^{4+}$ ($x = 0.2, 0.4, 0.6, 0.8, 1.0$, and 1.2 mol %) were synthesized by a high-temperature solid-state reaction method. The stoichiometric amounts of raw materials including BaCO_3 (analytical reagent, AR; Tianjin Dingshengxin Chemical Industry Co., Ltd), Gd_2O_3 (99.99%; Jining Tianyi New Materials Co., Ltd), Ta_2O_5 (99.5%; Aladdin Chemical Reagent Company), and MnCO_3 (AR; Tianjin Sailboats Chemical Reagent Co., Ltd) were weighed accurately and ground thoroughly in an agate mortar. Then, the obtained mixtures were presintered at 600°C for 3 h and then resintered at 1500°C for 6 h. Finally, the samples were cooled slowly to room temperature naturally in the furnace and ground again into powder for subsequent characterization.

4.2. Sample Characterizations. The X-ray diffraction (XRD) patterns of the samples were identified using a Bruker D8 X-ray diffractometer with a $\text{Cu K}\alpha$ radiation ($\lambda = 1.5406 \text{ \AA}$) in the range of $10\text{--}80^\circ$. The morphologies of the samples were characterized using a field-emission scanning electron microscope (FE-SEM; TESCAN MAIA3). The PL and PLE spectra, as well as the decay curves, of the as-obtained phosphors were plotted using an Edinburgh F55 spectrometer equipped with a 150 W continued-wavelength xenon lamp and a pulsed xenon lamp, respectively. The IQE values of the BGT:Mn^{4+} samples were measured using an Edinburgh F55 spectrometer equipped with an integrating sphere coated with BaSO_4 .

AUTHOR INFORMATION

Corresponding Author

*E-mail: huangxy04@126.com.

ORCID

Xiaoyong Huang: 0000-0003-4076-7874

Notes

The authors declare no competing financial interest.

ACKNOWLEDGMENTS

This work was supported by the National Natural Science Foundation of China (No. 51502190).

REFERENCES

- (1) Chen, J.; Yang, C.; Chen, Y.; He, J.; Liu, Z. Q.; Wang, J.; Zhang, J. Local Structure Modulation Induced Highly Efficient Far-Red Luminescence of $\text{La}_{1-x}\text{Lu}_x\text{AlO}_3:\text{Mn}^{4+}$ for Plant Cultivation. *Inorg. Chem.* **2019**, *58*, 8379–8387.
- (2) Li, M.; Zhang, X.; Zhang, H.; Chen, W.; Ma, L.; Wang, X.; Liu, Y.; Lei, B. Highly efficient and dual broad emitting light convertor: an option for next-generation plant growth LEDs. *J. Mater. Chem. C* **2019**, *7*, 3617–3622.
- (3) Shi, L.; Han, Y.-j.; Ji, Z.-x.; Zhang, Z.-w. Highly efficient and thermally stable $\text{CaYMGbO}_6:\text{Mn}^{4+}$ double perovskite red phosphor for indoor plant growth. *J. Mater. Sci.: Mater. Electron.* **2019**, *30*, 3107–3113.
- (4) Li, K.; Lian, H.; Van Deun, R.; Brik, M. G. A far-red-emitting $\text{NaMgLaTeO}_6:\text{Mn}^{4+}$ phosphor with perovskite structure for indoor plant growth. *Dyes Pigm.* **2019**, *162*, 214–221.
- (5) Ren, Y.; Cao, R.; Chen, T.; Su, L.; Cheng, X.; Chen, T.; Guo, S.; Yu, X. Photoluminescence properties of $\text{Ba}_2\text{LaSbO}_6:\text{Mn}^{4+}$ deep-red-emitting phosphor for plant growth LEDs. *J. Lumin.* **2019**, *209*, 1–7.
- (6) Zhou, Z.; Zhong, Y.; Xia, M.; Zhou, N.; Lei, B.; Wang, J.; Wu, F. Tunable dual emission of $\text{Ca}_3\text{Al}_4\text{ZnO}_{10}:\text{Bi}^{3+}, \text{Mn}^{4+}$ via energy transfer for indoor plant growth lighting. *J. Mater. Chem. C* **2018**, *6*, 8914–8922.
- (7) Huang, X.; Guo, H. Finding a novel highly efficient Mn^{4+} -activated $\text{Ca}_3\text{La}_2\text{W}_2\text{O}_{12}$ far-red emitting phosphor with excellent responsiveness to phytochrome P_{FR} : Towards indoor plant cultivation application. *Dyes Pigm.* **2018**, *152*, 36–42.
- (8) Li, K.; Lian, H.; Deun, R. V. Site occupancy and photoluminescence properties of a novel deep-red-emitting phosphor $\text{NaMgGdTeO}_6:\text{Mn}^{4+}$ with perovskite structure for w-LEDs. *J. Lumin.* **2018**, *198*, 155–162.
- (9) Zhong, J.; Chen, X.; Chen, D.; Liu, M.; Zhu, Y.; Li, X.; Ji, Z. A novel rare-earth free red-emitting $\text{Li}_3\text{Mg}_2\text{SbO}_6:\text{Mn}^{4+}$ phosphor-in-glass for warm w-LEDs: Synthesis, structure, and luminescence properties. *J. Alloys Compd.* **2019**, *773*, 413–422.
- (10) Zhu, G.; Li, Z.; Wang, C.; Wang, X.; Zhou, F.; Gao, M.; Xin, S.; Wang, Y. Highly Eu^{3+} ions doped novel red emission solid solution phosphors $\text{Ca}_{18}\text{Li}_3(\text{Bi}, \text{Eu})(\text{PO}_4)_{14}$: structure design, characteristic luminescence and abnormal thermal quenching behavior investigation. *Dalton Trans.* **2019**, *48*, 1624–1632.
- (11) Wang, B.; Lin, H.; Huang, F.; Xu, J.; Chen, H.; Lin, Z.; Wang, Y. Non-Rare-Earth $\text{BaMgAl}_{10-2x}\text{O}_{17}:\text{xMn}^{4+}, \text{xMg}^{2+}$: A Narrow-Band Red Phosphor for Use as a High-Power Warm w-LED. *Chem. Mater.* **2016**, *28*, 3515–3524.
- (12) Shi, L.; Han, Y.-j.; Wang, H.-x.; Shi, D.-c.; Geng, X.-y.; Zhang, Z.-w. High-efficiency and thermally stable far-red emission of Mn^{4+} in double cubic perovskite $\text{Sr}_3\text{Y}_2\text{W}_4\text{O}_{24}$ for plant cultivation. *J. Lumin.* **2019**, *208*, 307–312.
- (13) Pavitra, E.; Raju, G. S. R.; Ghoreishian, S. M.; Kwak, C. H.; Park, J. Y.; Han, Y.-K.; Huh, Y. S. Novel orange-emitting $\text{Ba}_2\text{LaNbO}_6:\text{Eu}^{3+}$ nanophosphors for NUV-based WLEDs and photocatalytic water purification. *Ceram. Int.* **2019**, *45*, 4781–4789.
- (14) Huang, X. Solid-state lighting: Red phosphor converts white LEDs. *Nat. Photonics* **2014**, *8*, 748–749.
- (15) Huang, X.; Wang, S.; Li, B.; Sun, Q.; Guo, H. High-brightness and high-color purity red-emitting $\text{Ca}_3\text{Lu}(\text{AlO})_3(\text{BO}_3)_4:\text{Eu}^{3+}$ phosphors with internal quantum efficiency close to unity for near-ultraviolet-based white-light-emitting diodes. *Opt. Lett.* **2018**, *43*, 1307–1310.
- (16) Huang, X. New red phosphors enable white LEDs to show both high luminous efficacy and color rendering index. *Sci. Bull.* **2019**, *64*, 879–880.
- (17) Huang, L.; Liu, Y.; Si, S.; Brik, M. G.; Wang, C.; Wang, J. A new reductive dl-mandelic acid loading approach for moisture-stable Mn^{4+} doped fluorides. *Chem. Commun.* **2018**, *54*, 11857–11860.
- (18) Zhu, Y.; Huang, L.; Zou, R.; Zhang, J.; Yu, J.; Wu, M.; Wang, J.; Su, Q. Hydrothermal synthesis, morphology and photoluminescent properties of a Mn^{4+} -doped novel red fluoride phosphor elpasolite K_2LiAlF_6 . *J. Mater. Chem. C* **2016**, *4*, 5690–5695.
- (19) Sasaki, T.; Fukushima, J.; Hayashi, Y.; Takizawa, H. Effects of Al- and Sn-substitution on photoluminescence properties of Mn^{4+} -doped spinel-type Mg_2TiO_4 phosphor. *J. Lumin.* **2017**, *187*, 540–545.
- (20) Sasaki, T.; Fukushima, J.; Hayashi, Y.; Takizawa, H. Synthesis and photoluminescence properties of Mn^{4+} -doped magnetoplumbite-related aluminate X-type $\text{Ca}_2\text{Mg}_2\text{Al}_{28}\text{O}_{46}$ and W-type $\text{CaMg}_2\text{Al}_{16}\text{O}_{27}$ red phosphors. *Ceram. Int.* **2017**, *43*, 7147–7152.
- (21) Sasaki, T.; Fukushima, J.; Hayashi, Y.; Takizawa, H. Synthesis and photoluminescence properties of a novel aluminosilicate $\text{Sr}_3\text{Al}_{10}\text{SiO}_{20}:\text{Mn}^{4+}$ red phosphor. *J. Lumin.* **2017**, *188*, 101–106.
- (22) Cai, P.; Qin, L.; Chen, C.; Wang, J.; Bi, S.; Kim, S. I.; Huang, Y.; Seo, H. J. Optical Thermometry Based on Vibration Sidebands in $\text{Y}_2\text{MgTiO}_6:\text{Mn}^{4+}$ Double Perovskite. *Inorg. Chem.* **2018**, *57*, 3073–3081.
- (23) Adachi, S. Photoluminescence properties of Mn^{4+} -activated oxide phosphors for use in white-LED applications: A review. *J. Lumin.* **2018**, *202*, 263–281.

- (24) Chen, D.; Zhou, Y.; Zhong, J. A review on Mn^{4+} activators in solids for warm white light-emitting diodes. *RSC Adv.* **2016**, *6*, 86285–86296.
- (25) Lin, H.; Hu, T.; Huang, Q.; Cheng, Y.; Wang, B.; Xu, J.; Wang, J.; Wang, Y. Non-Rare-Earth $K_2XF_7:Mn^{4+}$ ($X = Ta, Nb$): A Highly-Efficient Narrow-Band Red Phosphor Enabling the Application in Wide-Color-Gamut LCD. *Laser Photonics Rev.* **2017**, *11*, No. 1700148.
- (26) Hu, T.; Lin, H.; Lin, F.; Gao, Y.; Cheng, Y.; Xu, J.; Wang, Y. Narrow-band red-emitting $KZnF_3:Mn^{4+}$ fluoroperovskites: insights into electronic/vibronic transition and thermal quenching behavior. *J. Mater. Chem. C* **2018**, *6*, 10845–10854.
- (27) Lin, H.; Hu, T.; Cheng, Y.; Chen, M.; Wang, Y. Glass Ceramic Phosphors: Towards Long-Lifetime High-Power White Light-Emitting-Diode Applications-A Review. *Laser Photonics Rev.* **2018**, *12*, No. 1700344.
- (28) Hu, T.; Lin, H.; Cheng, Y.; Huang, Q.; Xu, J.; Gao, Y.; Wang, J.; Wang, Y. A highly-distorted octahedron with a C_{2v} group symmetry inducing an ultra-intense zero phonon line in Mn^{4+} -activated oxyfluoride $Na_2WO_2F_4$. *J. Mater. Chem. C* **2017**, *5*, 10524–10532.
- (29) Huang, L.; Liu, Y.; Yu, J.; Zhu, Y.; Pan, F.; Xuan, T.; Brik, M. G.; Wang, C.; Wang, J. Highly stable $K_2SiF_6:Mn^{4+}@K_2SiF_6$ composite phosphor with narrow red emission for white LEDs. *ACS Appl. Mater. Interfaces* **2018**, *10*, 18082–18092.
- (30) Huang, L.; Zhu, Y.; Zhang, X.; Zou, R.; Pan, F.; Wang, J.; Wu, M. HF-Free Hydrothermal Route for Synthesis of Highly Efficient Narrow-Band Red Emitting Phosphor $K_2Si_{1-x}F_6:xMn^{4+}$ for Warm White Light-Emitting Diodes. *Chem. Mater.* **2016**, *28*, 1495–1502.
- (31) Jin, Y.; Hu, Y.; Wu, H.; Duan, H.; Chen, L.; Fu, Y.; Ju, G.; Mu, Z.; He, M. A deep red phosphor $Li_2MgTiO_4:Mn^{4+}$ exhibiting abnormal emission: Potential application as color converter for warm w-LEDs. *Chem. Eng. J.* **2016**, *288*, 596–607.
- (32) Kim, D.; Park, S.; Choi, B. C.; Park, S. H.; Jeong, J. H.; Kim, J. H. The tetravalent manganese activated $SrLaMgTaO_6$ phosphor for w-LED applications. *Mater. Res. Bull.* **2018**, *97*, 115–120.
- (33) Kim, S. J.; Jang, H. S.; Unithrattil, S.; Kim, Y. H.; Im, W. B. Structural and luminescent properties of red-emitting $SrGe_4O_9:Mn^{4+}$ phosphors for white light-emitting diodes with high color rendering index. *J. Lumin.* **2016**, *172*, 99–104.
- (34) Huang, X.; Liang, J.; Li, B.; Sun, L.; Lin, J. High-efficiency and thermally stable far-red-emitting $NaLaMgWO_6:Mn^{4+}$ phosphors for indoor plant growth light-emitting diodes. *Opt. Lett.* **2018**, *43*, 3305–3308.
- (35) Cao, R.; Chen, T.; Ren, Y.; Chen, T.; Ao, H.; Li, W.; Zheng, G. Synthesis and photoluminescence properties of $Ca_2LaTaO_6:Mn^{4+}$ phosphor for plant growth LEDs. *J. Alloys Compd.* **2019**, *780*, 749–755.
- (36) Shi, L.; Han, Y.-j.; Zhang, Z.-g.; Ji, Z.-x.; Shi, D.-c.; Geng, X.-y.; Zhang, H.; Li, M.; Zhang, Z.-w. Synthesis and photoluminescence properties of novel $Ca_2LaSbO_6:Mn^{4+}$ double perovskite phosphor for plant growth LEDs. *Ceram. Int.* **2019**, *45*, 4739–4746.
- (37) Wang, S.; Sun, Q.; Devakumar, B.; Liang, J.; Sun, L.; Huang, X. Novel $Ca_2GdTbO_6:Mn^{4+},M$ ($M = Li^+, Na^+, K^+$, and Mg^{2+}) red phosphors for plant cultivation light-emitting diodes: Synthesis and luminescence properties. *J. Lumin.* **2019**, *214*, No. 116525.
- (38) Liang, J.; Devakumar, B.; Sun, L.; Sun, Q.; Wang, S.; Li, B.; Chen, D.; Huang, X. Mn^{4+} -activated $KLaMgWO_6$: A new high-efficiency far-red phosphor for indoor plant growth LEDs. *Ceram. Int.* **2019**, *45*, 4564–4569.
- (39) Sun, Q.; Wang, S.; Devakumar, B.; Sun, L.; Liang, J.; Huang, X. Mn^{4+} -activated $BaLaMgSbO_6$ double-perovskite phosphor: a novel high-efficiency far-red-emitting luminescent material for indoor plant growth lighting. *RSC Adv.* **2019**, *9*, 3303–3310.
- (40) Liang, J.; Devakumar, B.; Sun, L.; Sun, Q.; Wang, S.; Huang, X. Novel Mn^{4+} doped Ca_2GdSbO_6 red-emitting phosphor: A potential color converter for light-emitting diodes. *J. Am. Ceram. Soc.* **2019**, *102*, 4730–4736.
- (41) Sun, Q.; Wang, S.; Devakumar, B.; Li, B.; Sun, L.; Liang, J.; Huang, X. Synthesis and photoluminescence properties of novel far-red-emitting $BaLaMgNbO_6:Mn^{4+}$ phosphors for plant growth LEDs. *RSC Adv.* **2018**, *8*, 28538–28545.
- (42) Zheng, J.; Wang, S.; Gao, L.; Ma, Z.; Wang, F. First-principles calculations of crystal structure, electronic structure and optical properties of Ba_2RETaO_6 ($RE = Y, La, Pr, Sm, Gd$). *J. Mater. Sci.* **2018**, *53*, 9401–9410.
- (43) Wang, L.; Yuan, L.; Xu, Y.; Zhou, R.; Qu, B.; Ding, N.; Shi, M.; Zhang, B.; Chen, Y.; Jiang, Y.; Wang, D.; Shi, J. Luminescent properties of $La_2LiTaO_6:Mn^{4+}$ and its application as red emission LEDs phosphor. *Appl. Phys. A* **2014**, *117*, 1777–1783.
- (44) Xu, W.; Chen, D.; Yuan, S.; Zhou, Y.; Li, S. Tuning excitation and emission of Mn^{4+} emitting center in $Y_3Al_5O_{12}$ by cation substitution. *Chem. Eng. J.* **2017**, *317*, 854–861.
- (45) Li, K.; Mara, D.; Van Deun, R. Synthesis and luminescence properties of a novel dazzling red-emitting phosphor $NaSr_2SbO_6:Mn^{4+}$ for UV/n-UV w-LEDs. *Dalton Trans.* **2019**, *48*, 3187–3192.
- (46) Kim, M.; Park, W. B.; Lee, J.-W.; Lee, J.; Kim, C. H.; Singh, S. P.; Sohn, K.-S. $Rb_3SiF_7:Mn^{4+}$ and $Rb_2CsSiF_7:Mn^{4+}$ Red-Emitting Phosphors with a Faster Decay Rate. *Chem. Mater.* **2018**, *30*, 6936–6944.
- (47) Wu, Y.; Zhuang, Y.; Lv, Y.; Ruan, K.; Xie, R.-J. A high-performance non-rare-earth deep-red-emitting $Ca_{14-x}Sr_xZn_6Al_{10}O_{35}:Mn^{4+}$ phosphor for high-power plant growth LEDs. *J. Alloys Compd.* **2019**, *781*, 702–709.
- (48) Zhong, J.; Peng, Y.; Chen, D.; Liu, M.; Li, X.; Zhu, Y.; Ji, Z. Highly efficient rare-earth-free deep red emitting phosphor $La_2Li_{1-y}Sb_{1-x}O_6:xMn^{4+},yMg^{2+}$: application in high-power warm w-LEDs. *J. Mater. Chem. C* **2018**, *6*, 13305–13315.
- (49) Chen, W.; Cheng, Y.; Shen, L.; Shen, C.; Liang, X.; Xiang, W. Red-emitting $Sr_2MgGe_2O_7:Mn^{4+}$ phosphors: Structure, luminescence properties, and application in warm white light emitting diodes. *J. Alloys Compd.* **2018**, *762*, 688–696.
- (50) Zhou, Z.; Li, Y.; Xia, M.; Zhong, Y.; Zhou, N.; Hintzen, H. T. B. Improved luminescence and energy-transfer properties of $Ca_{14}Al_{10}Zn_6O_{35}:Ti^{4+},Mn^{4+}$ deep-red-emitting phosphors with high brightness for light-emitting diode (LED) plant-growth lighting. *Dalton Trans.* **2018**, *47*, 13713–13721.
- (51) Blasse, G. Energy transfer in oxido phosphors. *Phys. Lett. A* **1968**, *28*, 444–445.
- (52) Fu, A.; Zhou, L.; Wang, S.; Li, Y. Preparation, structural and optical characteristics of a deep red-emitting $Mg_2Al_4Si_5O_{18}:Mn^{4+}$ phosphor for warm w-LEDs. *Dyes Pigm.* **2018**, *148*, 9–15.
- (53) Yang, C.; Zhang, Z.; Hu, G.; Cao, R.; Liang, X.; Xiang, W. A novel deep red phosphor $Ca_{14}Zn_6Ga_{10}O_{35}:Mn^{4+}$ as color converter for warm W-LEDs: Structure and luminescence properties. *J. Alloys Compd.* **2017**, *694*, 1201–1208.
- (54) Cao, R.; Xiao, H.; Zhang, F.; Luo, Z.; Chen, T.; Li, W.; Liu, P.; Zheng, G. Red-emitting phosphor $Na_2Ca_2Nb_4O_{13}:Eu^{3+}$ for LEDs: Synthesis and luminescence properties. *J. Lumin.* **2019**, *208*, 350–355.
- (55) Deng, H.; Gao, Z.; Xue, N.; Jeong, J. H.; Yu, R. A novel Eu^{3+} -doped garnet-type tellurate red-emitting phosphor with high thermal stability and color purity. *J. Lumin.* **2017**, *192*, 684–689.
- (56) Jiang, G.; Yang, B.; Zhao, G.; Liu, Y.; Zou, J.; Sun, H.; Ou, H.; Fang, Y.; Hou, J. High quantum efficiency far red emission from double perovskite structured $CaLaMgMO_6:Mn^{4+}$ ($M = Nb, Ta$) phosphor for UV-based light emitting diodes application. *Opt. Mater.* **2018**, *83*, 93–98.
- (57) Zhong, J.; Chen, D.; Chen, X.; Wang, K.; Li, X.; Zhu, Y.; Ji, Z. Efficient rare-earth free red-emitting $Ca_2YSbO_6:Mn^{4+},M$ ($M = Li^+, Na^+, K^+, Mg^{2+}$) phosphors for white light-emitting diodes. *Dalton Trans.* **2018**, *47*, 6528–6537.
- (58) Chen, Y.; Wang, Q.; Mu, Z.; Feng, J.; Zhu, D.; Wu, F. Bi^{3+} and Mn^{4+} co-doped La_2MgGeO_6 blue-red tunable emission phosphors based on energy transfer for agricultural applications. *Optik* **2019**, *179*, 1035–1041.
- (59) Mo, F.; Lu, Z.; Zhou, L. Synthesis and luminescence properties of Mn^{4+} -activated Ba_2LaSbO_6 deep-red phosphor. *J. Lumin.* **2019**, *205*, 393–399.

(60) Chen, H.; Lin, H.; Huang, Q.; Huang, F.; Xu, J.; Wang, B.; Lin, Z.; Zhou, J.; Wang, Y. A novel double-perovskite $\text{Gd}_2\text{ZnTiO}_6\text{:Mn}^{4+}$ red phosphor for UV-based w-LEDs: structure and luminescence properties. *J. Mater. Chem. C* **2016**, *4*, 2374–2381.

(61) Li, X.; Chen, Z.; Wang, B.; Liang, R.; Li, Y.; Kang, L.; Liu, P. Effects of Impurity Doping on the Luminescence Performance of Mn^{4+} -Doped Aluminates with the Magnetoplumbite-Type Structure for Plant Cultivation. *Materials* **2019**, *12*, 86–96.

(62) Wu, C.; Li, J.; Xu, H.; Wu, J.; Zhang, J.; Ci, Z.; Feng, L.; Cao, C.; Zhang, Z.; Wang, Y. Preparation, structural and photoluminescence characteristics of novel red emitting $\text{Mg}_7\text{Ga}_2\text{GeO}_{12}\text{:Mn}^{4+}$ phosphor. *J. Alloys Compd.* **2015**, *646*, 734–740.

(63) Zhou, Z.; Zheng, J.; Shi, R.; Zhang, N.; Chen, J.; Zhang, R.; Suo, H.; Goldys, E. M.; Guo, C. Ab Initio Site Occupancy and Far-Red Emission of Mn^{4+} in Cubic-Phase $\text{La}(\text{MgTi})_{1/2}\text{O}_3$ for Plant Cultivation. *ACS Appl. Mater. Interfaces* **2017**, *9*, 6177–6185.

(64) Humayoun, U. B.; Tiruneh, S. N.; Yoon, D.-H. On the crystal structure and luminescence characteristics of a novel deep red emitting $\text{SrLaScO}_4\text{:Mn}^{4+}$. *Dyes Pigm.* **2018**, *152*, 127–130.

(65) Zhong, J.; Zhou, S.; Chen, D.; Li, J.; Zhu, Y.; Li, X.; Chen, L.; Ji, Z. Enhanced luminescence of a $\text{Ba}_2\text{GdSbO}_6\text{:Mn}^{4+}$ red phosphor via cation doping for warm white light-emitting diodes. *Dalton Trans.* **2018**, *47*, 8248–8256.

(66) Fu, A.; Pang, Q.; Yang, H.; Zhou, L. $\text{Ba}_2\text{YNbO}_6\text{:Mn}^{4+}$ -based red phosphor for warm white light-emitting diodes (WLEDs): Photoluminescent and thermal characteristics. *Opt. Mater.* **2017**, *70*, 144–152.